

## SEMICONDUCTORS

## High ambipolar mobility in cubic boron arsenide

Jungwoo Shin<sup>1†</sup>, Geethal Amila Gamage<sup>2†</sup>, Zhiwei Ding<sup>1†</sup>, Ke Chen<sup>1</sup>, Fei Tian<sup>2</sup>, Xin Qian<sup>1</sup>, Jiawei Zhou<sup>1</sup>, Hwijong Lee<sup>3</sup>, Jianshi Zhou<sup>3</sup>, Li Shi<sup>3</sup>, Thanh Nguyen<sup>4</sup>, Fei Han<sup>4</sup>, Mingda Li<sup>4</sup>, David Broido<sup>5</sup>, Aaron Schmidt<sup>1</sup>, Zhifeng Ren<sup>2\*</sup>, Gang Chen<sup>1\*</sup>

Semiconductors with high thermal conductivity and electron-hole mobility are of great importance for electronic and photonic devices as well as for fundamental studies. Among the ultrahigh-thermal conductivity materials, cubic boron arsenide (c-BAs) is predicted to exhibit simultaneously high electron and hole mobilities of >1000 centimeters squared per volt per second. Using the optical transient grating technique, we experimentally measured thermal conductivity of 1200 watts per meter per kelvin and ambipolar mobility of 1600 centimeters squared per volt per second at the same locations on c-BAs samples at room temperature despite spatial variations. Ab initio calculations show that lowering ionized and neutral impurity concentrations is key to achieving high mobility and high thermal conductivity, respectively. The high ambipolar mobilities combined with the ultrahigh thermal conductivity make c-BAs a promising candidate for next-generation electronics.

The performance of microelectronic and optoelectronic devices benefits from semiconductors with simultaneously high electron and hole mobilities and high thermal conductivity (1, 2). However, mobility and thermal conductivity measurements have thus far identified no such materials. Two of the most widely used semiconductors, silicon and gallium arsenide (GaAs), for example, have high room temperature (RT) electron mobilities of  $\mu_e = 1400 \text{ cm}^2\text{V}^{-1}\text{s}^{-1}$  and  $8500 \text{ cm}^2\text{V}^{-1}\text{s}^{-1}$ , respectively. However, their corresponding RT hole mobilities ( $\mu_h = 450 \text{ cm}^2\text{V}^{-1}\text{s}^{-1}$  for Si and  $400 \text{ cm}^2\text{V}^{-1}\text{s}^{-1}$  for GaAs) and thermal conductivities ( $\kappa_{\text{RT}} = 140 \text{ Wm}^{-1}\text{K}^{-1}$  for Si and  $45 \text{ Wm}^{-1}\text{K}^{-1}$  for GaAs) are lower than desired. Although graphene has high electron and hole mobilities and a high in-plane thermal conductivity, the cross-plane heat conduction is low (3, 4). Diamond has the highest RT thermal conductivity and excellent electron and hole mobilities; however, its large bandgap of 5.4 eV hinders its effective doping and utilization as a semiconductor material (5). Recently, first-principles calculations have predicted that cubic boron arsenide (c-BAs) should have exceptionally high RT thermal conductivity of  $\sim 1400 \text{ Wm}^{-1}\text{K}^{-1}$ , 10 times as high as that of Si. This high value stems from its unusual phonon dispersions and chemical bonding properties that promote simultaneously weak three-phonon and four-phonon scattering (6–8). This prediction has

now been demonstrated experimentally (9–11), with measured c-BAs thermal conductivities in the range of  $\kappa_{\text{RT}} = 1000$  to  $1300 \text{ Wm}^{-1}\text{K}^{-1}$ , identifying c-BAs as the most thermally conductive semiconductor other than diamond.

First-principles calculations have also predicted that c-BAs should have simultaneously high RT electron and hole mobilities of  $\mu_e = 1400 \text{ cm}^2\text{V}^{-1}\text{s}^{-1}$  and  $\mu_h = 2100 \text{ cm}^2\text{V}^{-1}\text{s}^{-1}$ , respectively (12). The major reason for such high electron and hole mobilities is the high energy and low occupation of polar optical phonons in c-BAs, which give rise to weak carrier scattering. This feature distinguishes c-BAs from other III-V semiconductors, which have high electron mobility but much lower hole mobility, where  $\mu_e/\mu_h > 10$  to  $\sim 100$  (13, 14), except for AlSb ( $\mu_e = 200 \text{ cm}^2\text{V}^{-1}\text{s}^{-1}$  and  $\mu_h = 400 \text{ cm}^2\text{V}^{-1}\text{s}^{-1}$ ).

Despite the promising theoretical predictions, experimental measurements have not found high mobilities in BAs. Similar to the history of the development of other III-V semiconductors (15), the initial quality of c-BAs crystals has been limited by large and non-uniform defect concentrations. Because traditional bulk transport measurement methods can only obtain the defect-limited behaviors instead of the intrinsic properties, the high defect densities in c-BAs crystals have prevented such measurements from assessing the validity of the predicted high mobilities. Furthermore, previous studies have shown that thermal conductivity and electronic mobility do not seem to have a strong relationship with each other. Kim *et al.* measured  $\kappa_{\text{RT}} = 186 \text{ Wm}^{-1}\text{K}^{-1}$  and estimated  $\mu_h = 400 \text{ cm}^2\text{V}^{-1}\text{s}^{-1}$  of a c-BAs microrod sample (16). Chen *et al.* measured  $\kappa_{\text{RT}} = 920 \text{ Wm}^{-1}\text{K}^{-1}$  and  $\mu_h = 22 \text{ cm}^2\text{V}^{-1}\text{s}^{-1}$  of millimeter-scale c-BAs crystals (17). The obtained mobilities are much lower than the calculated mobility and do not show a clear correlation with the measured thermal conductivity. The origins of (i) the discrepancy between ab initio calculations and experi-

ments and (ii) the decoupling between thermal and electrical properties have not been identified.

We used an optical transient grating (TG) method to measure electrical mobility and thermal conductivity on the same spot of c-BAs single crystals. Our experiments confirm that c-BAs has simultaneous high thermal conductivity and high electron and hole mobilities. Using ab initio calculations, we show that ionized impurities strongly scatter charge carriers, whereas neutral impurities are mainly responsible for the thermal conductivity reduction. These findings establish c-BAs as the only known semiconductor with this combination of desirable properties and place it among the ideal materials for next-generation microelectronics applications.

We prepared c-BAs samples using multistep chemical vapor transport with varying conditions (18) (figs. S1 and S2). We used scanning electron microscopy (SEM) to image a c-BAs single crystal with a thickness of  $\sim 20 \mu\text{m}$  (Fig. 1, A and B) and confirmed the cubic structure with x-ray diffraction (XRD) (Fig. 1C), in agreement with the literature (19).

We used photoluminescence (PL) and Raman spectroscopies to identify the nonuniform impurity distribution in c-BAs (17, 20). We measured the PL spectrum (Fig. 1D) and performed two-dimensional (2D) PL mapping of c-BAs crystals (Fig. 1E). Local bright spots indicate the spatial differences in charge carrier density and recombination dynamics. We also measured the Raman spectrum (Fig. 1F) and performed 2D Raman background scattering intensity ( $I_{\text{BG}}$ ) mapping (Fig. 1G). The strong Raman peak at  $\sim 700 \text{ cm}^{-1}$  is associated with the longitudinal optical (LO) mode of c-BAs at the zone center. The full width at half maximum of the LO peak and  $I_{\text{BG}}$  can be attributed to mass disorder resulting from impurities, responsible for large  $\kappa$  variation (11, 21).

We used the TG technique (22–24) (Fig. 2A) to simultaneously measure electrical and thermal transport on multiple spots (Fig. 1, circles a to d). Two femtosecond laser pulses (pump) with wavevectors  $\mathbf{k}_1$  and  $\mathbf{k}_2$  create sinusoidal optical interference on the c-BAs samples, exciting electron-hole pairs accordingly (fig. S3). A third laser pulse ( $\mathbf{k}_3$ ; probe) arrives at the sample spot after delay time  $t$ , which is subsequently diffracted to the direction of  $\mathbf{k}_1 - \mathbf{k}_2 + \mathbf{k}_3$  and mixed with a fourth pulse ( $\mathbf{k}_4$ ) for heterodyne detection. As the photoexcited carriers undergo diffusion and recombination, the corresponding diffraction signal decays with  $t$ . We show the calculated time-dependent electron-hole profile in c-BAs in Fig. 2B and figs. S4 and S5.

Diffusion and recombination of photoexcited carriers result in a fast exponential decay in the TG signal ( $t < 1$  ns), followed by a slower

<sup>1</sup>Department of Mechanical Engineering, Massachusetts Institute of Technology, Cambridge, MA 02139, USA.

<sup>2</sup>Department of Physics and Texas Center for Superconductivity, University of Houston, Houston, TX 77204, USA. <sup>3</sup>Materials Science and Engineering Program, The University of Texas at Austin, Austin, TX 78712, USA. <sup>4</sup>Department of Nuclear Science and Engineering, Massachusetts Institute of Technology, Cambridge, MA 02139, USA. <sup>5</sup>Department of Physics, Boston College, Chestnut Hill, MA 02467, USA.

\*Corresponding author. Email: zren2@central.uh.edu (Z.R.); gchen2@mit.edu (G.C.)

†These authors contributed equally to this work.

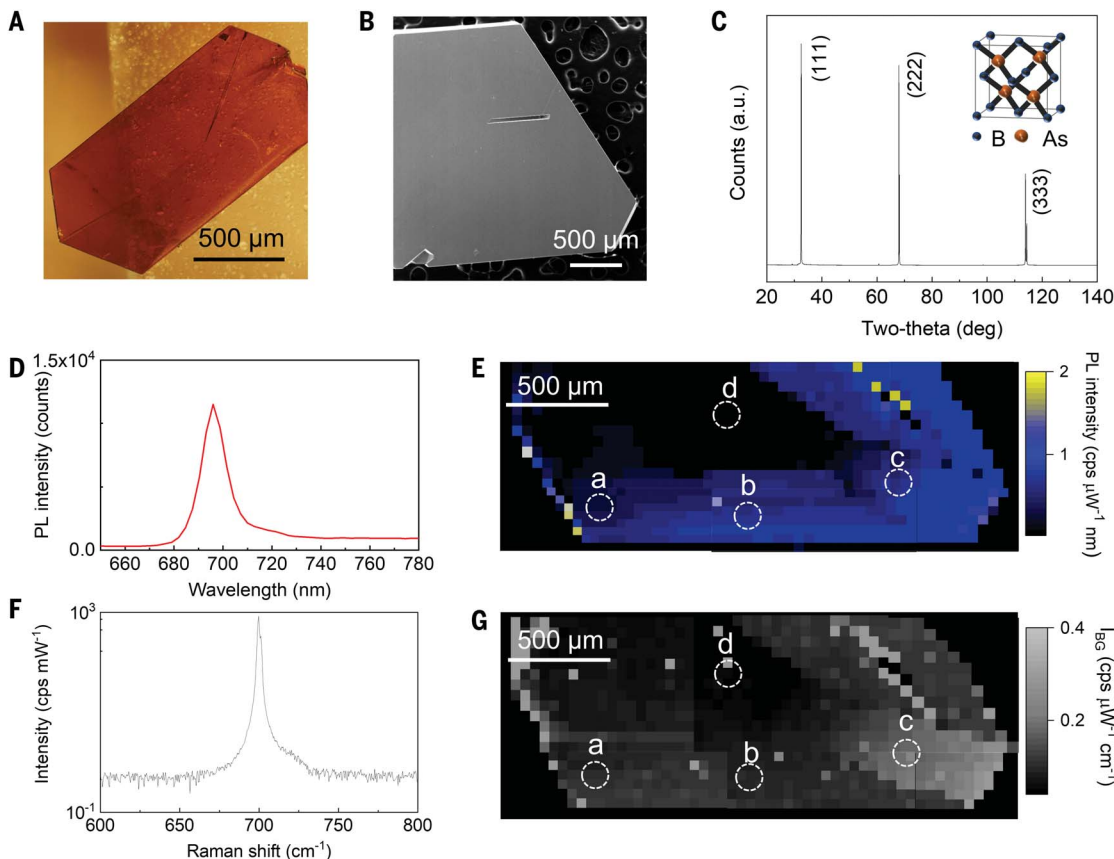


**Fig. 1. Optical characterization of c-BAs single crystals.** (A) Optical photograph. (B) SEM image. (C) XRD. a.u., arbitrary units; deg, degrees. (D and E) A typical PL spectrum (D) and 2D PL intensity mapping (E) integrated over 100-nm spectrum range for each spot. The dashed circles show TG measurement spots (a to d). cps, counts per second. (F and G) A typical Raman spectrum (F) and 2D mapping of background Raman scattering intensity (G) integrated over 100  $\text{cm}^{-1}$  for each spot.

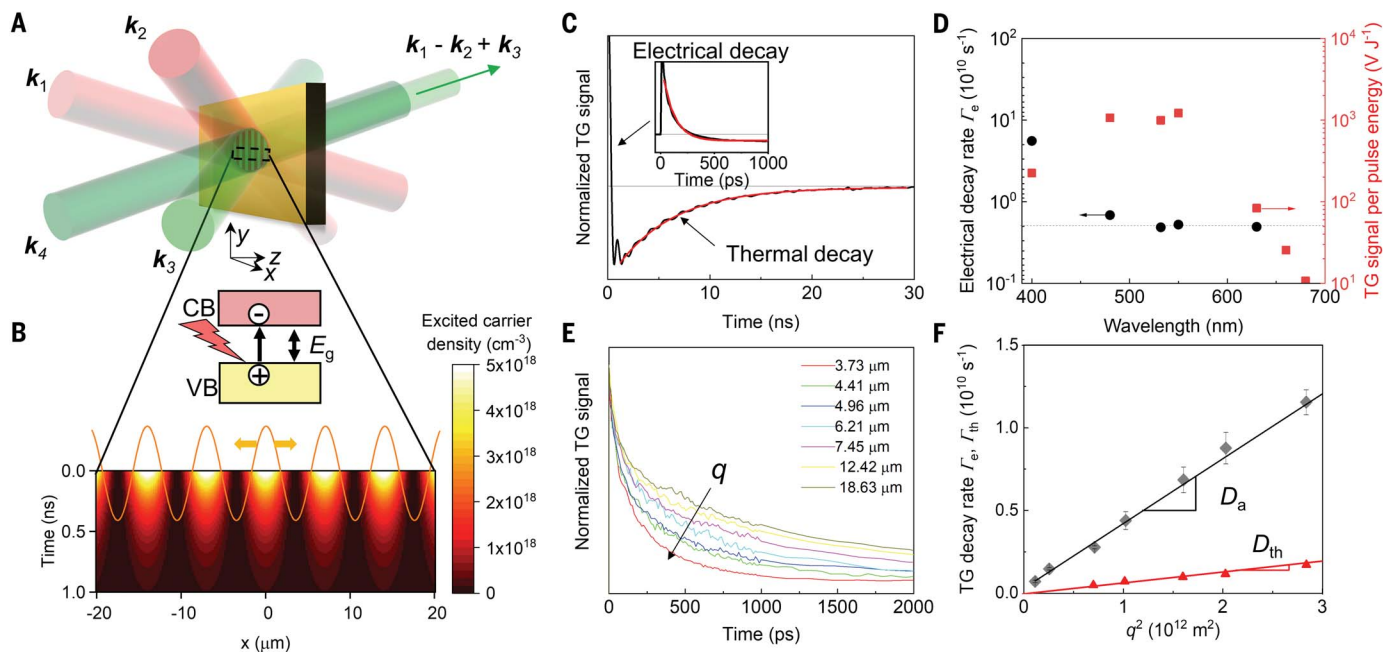


**Fig. 2. Thermal and electron transport measurements.** (A) Schematic illustration of TG experiments. (B) Calculated time-dependent electron-hole pair density in c-BAs. CB, conduction band; VB, valence band;  $E_g$ , bandgap. (C) TG signal for c-BAs. Thermal conductivity is calculated from exponential fitting (red line). (D) Wavelength-dependent electrical decay rate  $\Gamma_e$  and TG peak amplitude. (E) TG signal with varying diffraction grating periods  $q$ . (F) Electrical decay rate ( $\Gamma_e$ ) and thermal decay rate ( $\Gamma_{th}$ ) versus  $q^2$ . Error bars show experimental uncertainties.

Downloaded from https://www.science.org on July 22, 2022

thermal decay ( $t > 1$  ns) with an opposite sign (Fig. 2C). The short and long time decays are used to calculate charge carrier mobility and thermal conductivity on the same spot, respectively (see fig. S6 for details). Thermal conductivity is directly calculated from the exponential fitting of the long time decay (red line). The electrical decay is sensitive to the wavelength of the pump pulses. We use an optical parametric amplifier (OPA) to match the wavelength of the pump beam with the bandgap (2.02 eV) of c-BAs to avoid excitation of high-energy electrons that can lead to hot electrons and holes with different scattering dynamics and mobilities (25). We also determined the wavelength-dependent electrical decay rate  $\Gamma_e$  and the lock-in amplifier amplitude of the TG peak (Fig. 2D). TG decays much faster at shorter wavelengths ( $\lambda < 500$  nm) and reaches a plateau near the bandgap ( $\lambda \sim 600$  nm) followed by signal loss for photon energy below the bandgap ( $\lambda > 650$  nm) (fig. S7). The slopes of electrical decay  $\Gamma_e$  and thermal decay  $\Gamma_{th}$  versus  $q^2$  (Fig. 2, E and F) are equivalent to the ambipolar diffusivity  $D_a$  and thermal diffusivity  $D_{th}$  of c-BAs.  $D_a$  is subsequently converted to ambipolar mobility  $\mu_a = eD_a/k_B T = 2\mu_{dir}/(\mu_e + \mu_h)$ , which is dominated by the low mobility carrier, where  $k_B$  is the Boltzmann constant,  $e$  is the elementary charge, and  $T$  is temperature.

We measured a wide variation of the RT  $\kappa$  and  $\mu_a$  for spots a to d (a:  $920 \text{ W m}^{-1} \text{ K}^{-1}$  and  $731 \text{ cm}^2 \text{ V}^{-1} \text{ s}^{-1}$ ; b:  $1132 \text{ W m}^{-1} \text{ K}^{-1}$  and  $1482 \text{ cm}^2 \text{ V}^{-1} \text{ s}^{-1}$ ; c:  $163 \text{ W m}^{-1} \text{ K}^{-1}$  and  $331 \text{ cm}^2 \text{ V}^{-1} \text{ s}^{-1}$ ; d:  $211 \text{ W m}^{-1} \text{ K}^{-1}$  and  $328 \text{ cm}^2 \text{ V}^{-1} \text{ s}^{-1}$ ). This large spatial variation of thermal and electrical properties can be attributed to corresponding variations in impurity density. A higher impurity density lowers PL intensity and increases  $I_{BG}$ . To corroborate this trend, we intentionally doped c-BAs with C (batch IV) and measured  $\kappa = 200$  to  $953 \text{ W m}^{-1} \text{ K}^{-1}$  and  $\mu_a = 195$  to  $416 \text{ cm}^2 \text{ V}^{-1} \text{ s}^{-1}$  along with large variation in  $I_{BG}$  and low PL intensity (figs. S8 and S9).

Common impurities in c-BAs are group IV elements, such as C and Si. These impurities can serve as electron acceptors in c-BAs because of low formation energies (26). Space charges created by ionized impurities introduce distortions in the local bonding environment, driving distinct phonon scattering mechanisms. The  $\kappa$  of c-BAs can be calculated by solving the phonon Boltzmann transport equation, including three- and four-phonon scattering and phonon-scattering by neutral (solid lines) and charged (dashed lines) group IV impurities on B or As sites (27, 28) (Fig. 3A). Our calculated  $\kappa$  decreases with increasing mass difference between the impurity and host atoms. Upon impurity ionization, the number of valence electrons of the impurity (IV) matches that of B or As (III or V), resulting in weaker bond perturbations than those from the

neutral impurities. Consequently, the thermal conductivity reduction from ionized impurities is smaller than that caused by the un-ionized impurities, especially when the substituted impurity has a similar mass to that of the host atom—i.e.,  $\text{Ge}_{As}^-$  and  $\text{C}_B^+$ .

The bond perturbation and Coulomb potential of impurities modify electron and hole transport dynamics in c-BAs differently. Building on recent developments in computing formation energies for charged impurities (29), we used ab initio calculations to study the effect of group IV impurities on the RT  $\mu_a$  of c-BAs (Fig. 3B). We show electron-phonon scattering and long- and short-range defect scattering for holes in c-BAs with  $\text{Si}_{As}^-$  (see fig. S10 for details) (Fig. 3C). Long-range Coulombic interaction with charged impurities is found to be the dominant scattering mechanism near the band edge. The lack of a Coulomb potential for neutral impurities results in a weaker carrier scattering, causing  $\mu_a$  to not decrease until the concentration approaches  $10^{18} \text{ cm}^{-3}$ , where the electron-neutral impurity scattering starts to show an effect. However,  $\mu_a$  decreases mark-

edly with charged impurities from  $10^{16} \text{ cm}^{-3}$ , regardless of the mass of the impurity.

We elucidated the different effects of neutral and charged impurities on  $\kappa$  and  $\mu_a$  (Fig. 3D). Neutral impurities more strongly suppress  $\kappa$  because of stronger bond perturbations compared with those in charged impurities (27). Charged impurities predominantly contribute to  $\mu_a$  reduction regardless of their mass as a result of Coulombic scattering. Charged impurities with masses similar to that of the host atom would exhibit  $\kappa_{RT}$  above  $1000 \text{ W m}^{-1} \text{ K}^{-1}$ , even at a high impurity density of  $10^{19} \text{ cm}^{-3}$ , and  $\mu_a$  is significantly reduced to below  $400 \text{ cm}^2 \text{ V}^{-1} \text{ s}^{-1}$  at a moderate level of  $10^{18} \text{ cm}^{-3}$ .

We can also highlight the contrasting trends in  $\kappa$  and  $\mu_a$  with neutral and charged impurities from batches 0 to IV (Fig. 4A and table S1) (18). Solid and dashed lines in Fig. 4 show the trajectories of the calculated  $\mu_a$  and  $\kappa$  with neutral  $\text{Si}_{As}^0$  and charged  $\text{Si}_{As}^-$  from  $10^{16}$  to  $10^{20} \text{ cm}^{-3}$ , respectively. Scattered points are the measured  $\mu_a$  and  $\kappa$  values of samples from different batches, labeled with different colors. All measured data fit into the area between

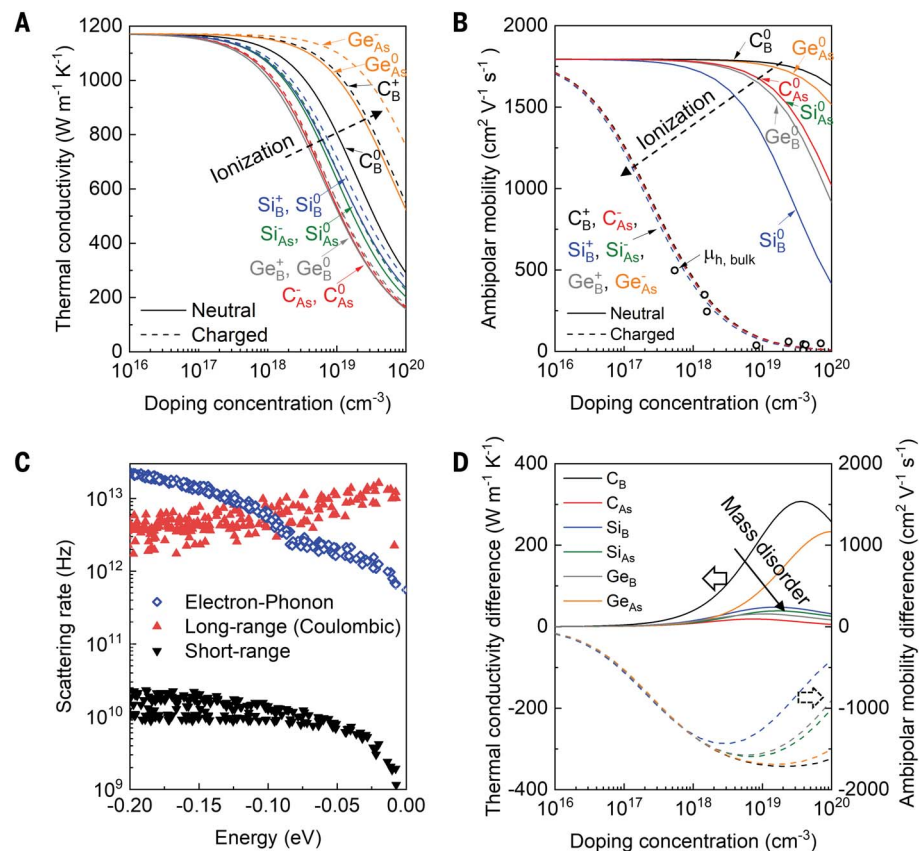
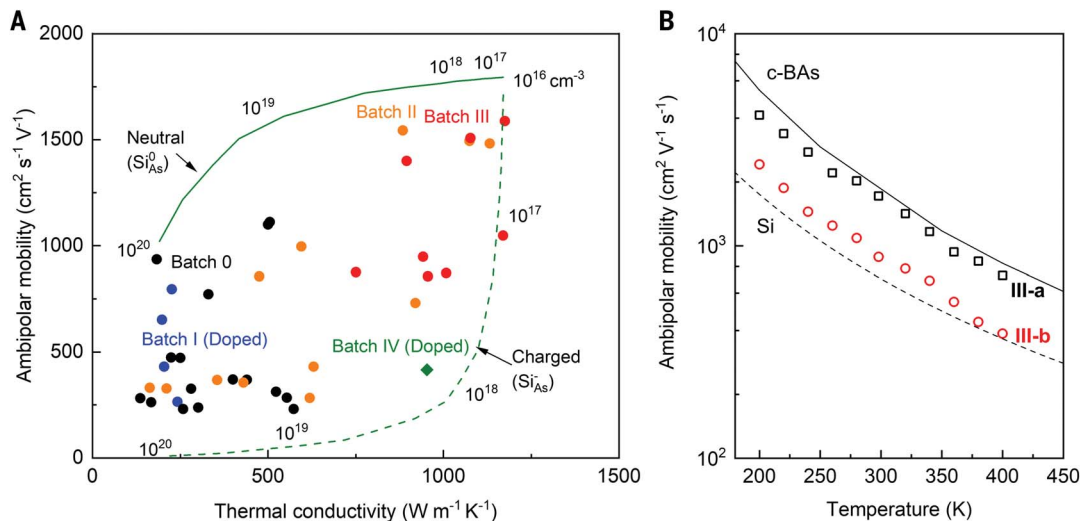


**Fig. 3. Theoretical calculation of the impurity effects on thermal conductivity and mobility.** (A and B) Calculated thermal conductivity (A) and ambipolar mobility (B) with neutral (solid lines) and charged (dashed lines) group IV impurities. Open circles are  $\mu_h$  values of bulk samples measured by electrical probes (fig. S12). (C) Calculated electron-phonon and short- and long-range impurity scattering rates for holes. Zero of energy is at the valence band maximum. ( $\text{Si}_{As}^- = 10^{18} \text{ cm}^{-3}$ ). (D) Thermal conductivity (solid lines) and mobility (dashed lines) differences between charged and neutral impurities.

**Fig. 4. Ambipolar mobility and thermal conductivity of c-BAs.**

**(A)** Measured mobility and thermal conductivity of c-BAs from different batches (batches **0**, **I**, **II**, **III**, and **IV**). See table S1 for details. The solid and dashed lines show the calculated  $\mu_a$  and  $\kappa$  with varying concentrations of neutral  $\text{Si}_{\text{As}}^0$  and charged  $\text{Si}_{\text{As}}^-$ , respectively. Typical uncertainties for  $\mu_a$  and  $\kappa$  are 11%. **(B)** Temperature-dependent ambipolar mobility of c-BAs (**III-a** and **III-b**). The solid and dashed lines show calculated  $\mu_a$  of pristine c-BAs and Si, respectively (32).



the trajectory curves. Among the high-quality c-BAs batch (**III**), we measure  $\mu_a = 1600 \pm 170 \text{ cm}^2 \text{V}^{-1} \text{s}^{-1}$  and  $\kappa = 1200 \pm 130 \text{ Wm}^{-1} \text{K}^{-1}$ . We measured the temperature-dependent  $\mu_a$  of two different spots (**III-a** and **III-b**) of high-quality samples (fig. S11). Our measured  $\mu_a$  for **III-a** shows good agreement with calculations (Fig. 4B). Hall measurements of the bulk samples provide  $\mu_h$  and carrier concentration  $p$  averaged over the entire sample with spatially varied impurity concentration. The measured bulk  $\mu_h$  plotted in Fig. 3B (see fig. S12 for details) is limited by the average impurity concentrations rather than local spots with low impurities.

The high-spatial resolution TG measurements provide clear evidence of simultaneously high electron and hole mobilities in c-BAs and demonstrate that through the elimination of defects and impurities, c-BAs could exhibit both high thermal conductivity and high electron and hole mobilities. Additionally, the observed weak correlation between the local thermal conductivity and mobility is caused by the different effects that neutral and ionized impurities have on these quantities. This notable combination of electronic and thermal properties, along with a thermal expansion coefficient and lattice constant that are closely matched to common semiconductors such as Si and GaAs (30, 31), make c-BAs a promising material for integrating with current and future semiconductor manufacturing processes and addressing the grand

challenges in thermal management for next-generation electronics.

#### REFERENCES AND NOTES

- X. Qian, J. Zhou, G. Chen, *Nat. Mater.* **20**, 1188–1202 (2021).
- G. Chen, *Nat. Rev. Phys.* **3**, 555–569 (2021).
- K. S. Novoselov *et al.*, *Science* **306**, 666–669 (2004).
- A. A. Balandin *et al.*, *Nano Lett.* **8**, 902–907 (2008).
- C. J. H. Wort, R. S. Balmer, *Mater. Today* **11**, 22–28 (2008).
- L. Lindsay, D. A. Broido, T. L. Reinecke, *Phys. Rev. Lett.* **111**, 025901 (2013).
- D. A. Broido, L. Lindsay, T. L. Reinecke, *Phys. Rev. B* **88**, 214303 (2013).
- T. L. Feng, L. Lindsay, X. L. Ruan, *Phys. Rev. B* **96**, 161201 (2017).
- J. S. Kang, M. Li, H. Wu, H. Nguyen, Y. Hu, *Science* **361**, 575–578 (2018).
- F. Tian *et al.*, *Science* **361**, 582–585 (2018).
- S. Li *et al.*, *Science* **361**, 579–581 (2018).
- T. H. Liu *et al.*, *Phys. Rev. B* **98**, 081203 (2018).
- D. L. Rode, *Phys. Rev. B* **3**, 3287–3299 (1971).
- A. Nainani, B. R. Bennett, J. B. Boos, M. G. Ancona, K. C. Saraswat, *J. Appl. Phys.* **111**, 103706 (2012).
- J. I. Pankove, T. D. Moustakas, *Semicond. Semimet.* **50**, 1–10 (1997).
- J. Kim *et al.*, *Appl. Phys. Lett.* **108**, 201905 (2016).
- X. Chen *et al.*, *Chem. Mater.* **33**, 6974–6982 (2021).
- Materials and methods are available as supplementary materials online.
- J. A. Perri, S. Laplaca, B. Post, *Acta Cryst.* **11**, 310 (1958).
- S. Yue *et al.*, *Mater. Today Phys.* **13**, 100194 (2020).
- A. Rai, S. Li, H. L. Wu, B. Lv, D. G. Cahill, *Phys. Rev. Mater.* **5**, 013603 (2021).
- A. A. Maznev, T. F. Crimmins, K. A. Nelson, *Opt. Lett.* **23**, 1378–1380 (1998).
- A. A. Maznev, K. A. Nelson, J. A. Rogers, *Opt. Lett.* **23**, 1319–1321 (1998).
- S. Huberman *et al.*, *Science* **364**, 375–379 (2019).
- K. Chen *et al.*, *Carbon* **107**, 233–239 (2016).
- J. L. Lyons *et al.*, *Appl. Phys. Lett.* **113**, 251902 (2018).
- M. Fava *et al.*, *Npj Comput. Mater.* **7**, 54 (2021).
- M. Fava *et al.*, How dopants limit the ultrahigh thermal conductivity of boron arsenide: A first principles study, version 1, Zenodo (2021); <https://doi.org/10.5281/zenodo.4453192>.

- C. Freysoldt *et al.*, *Rev. Mod. Phys.* **86**, 253–305 (2014).
- F. Tian *et al.*, *Appl. Phys. Lett.* **114**, 131903 (2019).
- X. Chen *et al.*, *Phys. Rev. Appl.* **11**, 064070 (2019).
- N. D. Arora, J. R. Hauser, D. J. Roulston, *IEEE Trans. Electron Dev.* **29**, 292–295 (1982).

#### ACKNOWLEDGMENTS

**Funding:** This work was supported by the Office of Naval Research under Multidisciplinary University Research Initiative grant N00014-16-1-2436. This work made use of the MRSEC Shared Experimental Facilities at MIT, supported by the National Science Foundation under award no. DMR-1419807. **Author contributions:** Conceptualization: J.S., G.A.G., K.C., Z.R., and G.C. Materials preparation: G.A.G. and F.T. TG experiments: J.S. and K.C. TG modeling: J.S., K.C., X.Q., and G.C. Time-domain thermoreflectance, frequency-domain thermoreflectance, PL, and Raman measurements: J.S. Hall measurements: H.L., Jian.Z., L.S., T.N., F.H., and M.L. Mobility calculations: Z.D. and Jiaw.Z. Data analysis: J.S., G.A.G., Z.D., K.C., D.B., Z.R., and G.C. Funding and project administration: Z.R. and G.C. Supervision: Z.R. and G.C. Writing – original draft: J.S., G.A.G., Z.D., Z.R., and G.C. Review & editing: all authors. **Competing interests:** US patent publication no. 20210269318 has been granted to the method for growing c-BAs crystals presented in this work. A patent application on the high mobility of Bas, entitled “Ultra-high ambipolar mobility in cubic arsenide,” has been filed with the US Patent Office. The authors declare no other competing interests. **Data and materials availability:** All data are available in the main text and supplementary materials. **License information:** Copyright © 2022 the authors, some rights reserved; exclusive licensee American Association for the Advancement of Science. No claim to original US government works. <https://www.science.org/about/science-licenses-journal-article-reuse>

#### SUPPLEMENTARY MATERIALS

[science.org/doi/10.1126/science.abn4290](https://doi.org/10.1126/science.abn4290)  
Materials and Methods  
Supplementary Text  
Figs. S1 to S12  
Table S1  
References (33–55)

Submitted 1 December 2021; accepted 16 June 2022  
10.1126/science.abn4290

## High ambipolar mobility in cubic boron arsenide

Jungwoo ShinGeethal Amila GamageZhiwei DingKe ChenFei TianXin QianJiawei ZhouHwijong LeeJianshi ZhouLi ShiThanh NguyenFei HanMingda LiDavid BroidoAaron SchmidtZhiheng RenGang Chen

*Science*, 377 (6604), • DOI: 10.1126/science.abn4290

### Swift carriers

Boron arsenide is a semiconductor with several interesting properties, including a high thermal conductivity. Theoretical calculations also suggest that it has high ambipolar mobility, a measure of the mobility of electrons and holes. Yue *et al.* and Shin *et al.* used different types of measurements to observe a high ambipolar mobility in very pure cubic boron arsenide. Shin *et al.* were able to simultaneously measure the high thermal and electrical transport properties in the same place in their samples. Yue *et al.* found even higher ambipolar mobility than the theoretical estimates at a few locations. Boron arsenide's combination of transport properties could make it an attractive semiconductor for various applications. —BG

### View the article online

<https://www.science.org/doi/10.1126/science.abn4290>

### Permissions

<https://www.science.org/help/reprints-and-permissions>

Use of this article is subject to the [Terms of service](#)

*Science* (ISSN ) is published by the American Association for the Advancement of Science. 1200 New York Avenue NW, Washington, DC 20005. The title *Science* is a registered trademark of AAAS.

Copyright © 2022 The Authors, some rights reserved; exclusive licensee American Association for the Advancement of Science. No claim to original U.S. Government Works